

Defects and persistent luminescence in Eu-doped SrAl_2O_4

Khang Hoang*

Center for Computationally Assisted Science and Technology & Department of Physics,
North Dakota State University, Fargo, North Dakota 58108, United States

(Dated: November 9, 2022)

We investigate native point defects and rare-earth (co)dopants in SrAl_2O_4 using hybrid density-functional defect calculations. Europium (Eu) and dysprosium (Dy) are found to be mixed valence and energetically most favorable at the Sr lattice sites. However, unlike Eu where both Eu^{2+} and Eu^{3+} can be realized in synthesis, Dy is stable predominantly as Dy^{3+} , and the divalent Dy^{2+} may only be photogenerated under irradiation. On the basis of an analysis of Eu-related band-defect (including charge-transfer) and interconfigurational $5d-4f$ optical transitions, we assign the characteristic broad blue (445 nm) and green (520 nm) emission bands in Eu^{2+} -doped SrAl_2O_4 to the $4f^65d^1 \rightarrow 4f^7$ transition in Eu^{2+} incorporated at the Sr1 and Sr2 sites, respectively. Strontium interstitials (*not* oxygen vacancies, in contrast to what is commonly believed) and Dy_{Sr} can act as efficient electron traps for room-temperature persistent luminescence. This work calls for a re-assessment of certain assumptions regarding specific carrier trapping centers made in all mechanisms previously proposed for the persistent luminescence in Eu- and (Eu,Dy)-doped SrAl_2O_4 . It also serves as a methodological template for the understanding and design of rare-earth doped phosphors.

I. INTRODUCTION

Persistent luminescence, previously often referred to as phosphorescence or long-lasting phosphorescence, is an intriguing phenomenon in which a material re-emits light over long periods of time after the excitation has stopped [1, 2]. Persistent luminescent materials (or persistent phosphors) have numerous applications and potential applications in safety signage and toys, road markings, solid-state lighting (flicker reduction), bio-imaging, nighttime solar energy, and photocatalysis [3]. Scientific research on persistent luminescence really took off since the discovery of (Eu,Dy)-doped SrAl_2O_4 by Murayam, Takeuchi, Aoki, and Matsuzawa of Nemoto & Co., Ltd. (Japan) in 1993; the material was found to produce extremely bright green and long-lasting (over many hours) luminescence in the dark [4, 5]. Three decades after the seminal work of the Nemoto researchers, although there has been great progress in understanding the phenomenon and in discovering new persistent phosphors—as it has already been documented in many excellent review articles and book chapters published in the last several years [1–3, 6–8], details of the underlying mechanism for the persistent luminescence observed in rare-earth (RE) doped SrAl_2O_4 and similar materials are still under debate, and the search for new or improved persistent phosphors, in general, remains largely trial and error.

The optical properties of Eu-doped SrAl_2O_4 are characterized by a broad green emission band peaking at 520 nm at room temperature [9–11]. At lower temperatures, another peak occurs in the emission spectrum at 450 nm (blue) [12]. In addition, a broader excitation band peaking at 276 nm or 250 nm and sharp Eu^{3+} $4f-4f$ transitions in the excitation and emission spectra have also been reported [13–15]. Co-doping the material with Dy

does not change the emission spectrum, but strongly enhances the afterglow time and intensity [5]. There are currently about a dozen different mechanisms proposed in the literature to explain the persistent luminescence observed in Eu- and (Eu,Dy)-doped SrAl_2O_4 [5, 16–23]. All these mechanisms involve defect levels induced by the RE (co)dopants and/or native point defects. Oxygen vacancies, in particular, have been invoked in many mechanisms as electron trapping centers responsible for the delayed emission. Figure 1 shows a currently generally accepted mechanism involving electron trapping and detrapping processes (a mechanism involving hole trapping and detrapping is similar) [2]. In the context of Eu^{2+} -doped SrAl_2O_4 , the emission center is expected to be Eu^{2+} with the ground and excited states being $4f^7$ and $4f^65d^1$, respectively, and the trapping center can be native defects and/or RE co-dopants or other impurities.

Due to the lack of a detailed understanding of defect physics in SrAl_2O_4 , all the proposed mechanisms [5, 16–23] are highly speculative about specific emission centers and charge carrier trapping centers. This has been a *major obstacle* toward rational design of persistent phosphors with improved performance. Here, we present an investigation of native defects and RE (co)dopants in monoclinic SrAl_2O_4 using first-principles defect calculations. The hybrid density-functional theory (DFT)/Hartree-Fock method [24] employed here has been shown to be successful in the study of defects in semiconductors and insulators in general [25] and RE-doped materials in particular [26–28]. On the basis of our results, we identify dominant native defects, discuss the stable valence states of the RE (co)dopants, and determine all energy levels induced by the defects. Eu-related optical transitions, including band-defect and interconfigurational Eu^{2+} $5d-4f$ absorption and emission processes, are investigated to identify sources of the broad absorption and emission bands observed in experiments, including the characteristic blue and green emissions.

* khang.hoang@ndsu.edu

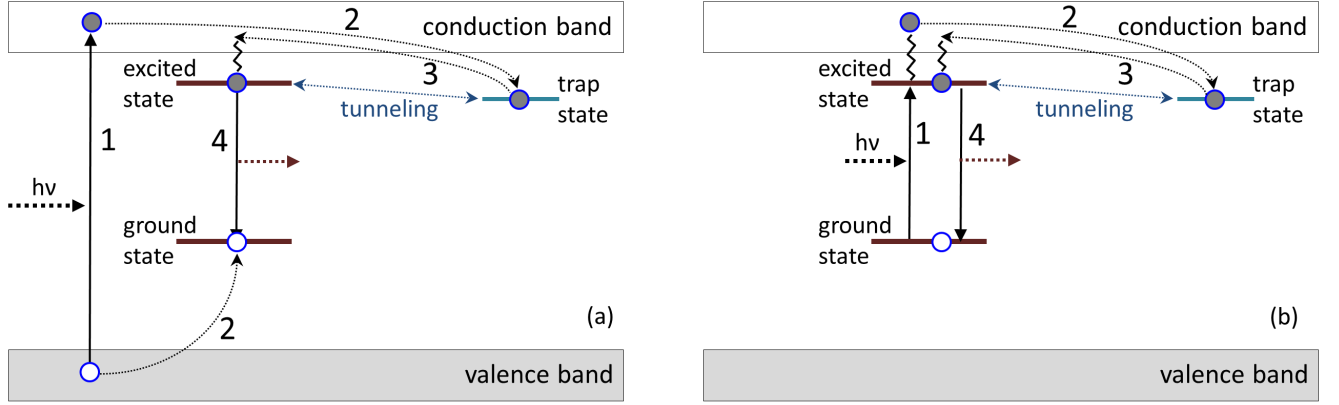


FIG. 1. Schematic illustration of a persistent luminescence mechanism under (a) band-to-band or (b) below-gap excitation: (1) excitation: electrons are excited and holes generated under illumination; (2) trapping: the excited electrons (generated holes) are captured nonradiatively by electron (hole) traps through the conduction (valence) band and/or via quantum tunneling; (3) detrapping: the trapped electrons are released under thermal stimulation; (4) recombination: the released electrons return to the emission center and recombine with holes, resulting in a delayed luminescence. Adapted from Xu and Tanabe [2]

II. METHODOLOGY

We model defects (i.e., native point defects and impurities) in SrAl_2O_4 using a supercell approach in which a defect is included in a periodically repeated finite volume of the host material. The formation energy of a defect X in effective charge state q (with respect to the host lattice) is defined as [25, 29]

$$E^f(X^q) = E_{\text{tot}}(X^q) - E_{\text{tot}}(\text{bulk}) - \sum_i n_i \mu_i + q(E_v + \mu_e) + \Delta^q, \quad (1)$$

where $E_{\text{tot}}(X^q)$ and $E_{\text{tot}}(\text{bulk})$ are the total energies of the defect-containing and perfect bulk supercells, respectively; n_i is the number of atoms of species i that have been added ($n_i > 0$) or removed ($n_i < 0$) to form the defect; μ_i is the atomic chemical potential, representing the energy of the reservoir with which atoms are being exchanged, and referenced to the total energy per atom of i in its elemental phase at 0 K. μ_e is the chemical potential of electrons, i.e., the Fermi level, representing the energy of the electron reservoir, referenced to the valence-band maximum (VBM) in the bulk (E_v). Finally, Δ^q is the correction term to align the electrostatic potentials of the bulk and defect supercells and to account for finite-size effects on the total energies of charged defects [30, 31].

Under thermodynamic equilibrium, the concentration of a defect is directly related to its formation energy [29]:

$$c = N_{\text{sites}} N_{\text{config}} \exp\left(\frac{-E^f}{k_B T}\right), \quad (2)$$

where N_{sites} is the number of high-symmetry sites in the lattice (per unit volume) on which the defect can be incorporated, N_{config} is the number of equivalent configurations (per site), and k_B is the Boltzmann constant. At

a given temperature, a defect with a lower formation energy occurs with a higher concentration. Note, however, that when a material is prepared under non-equilibrium conditions excess defects can be frozen-in and the equilibrium concentration is only the lower bound.

While the Fermi level in Eq. (1) can be treated as a variable, it is not a free parameter. The actual Fermi-level position of the material can be determined by solving the charge-neutrality equation [29]:

$$\sum_i c_i q_i - n_e + n_h = 0, \quad (3)$$

where c_i and q_i are the concentration and charge, respectively, of defect X_i ; n_e and n_h are free electron and hole concentrations, respectively; and the summation is over all possible defects present in the material.

The *thermodynamic* transition level between charge states q and q' of a defect, $\epsilon(q/q')$, is defined as the Fermi-level position at which the formation energy of the defect in charge state q is equal to that in state q' [25], i.e.,

$$\epsilon(q/q') = \frac{E^f(X^q; \mu_e = 0) - E^f(X^{q'}; \mu_e = 0)}{q' - q}, \quad (4)$$

where $E^f(X^q; \mu_e = 0)$ is the formation energy of the defect X in charge state q when the Fermi level is at the VBM ($\mu_e = 0$). This $\epsilon(q/q')$ level [also referred to as the (q/q') level], corresponding to a defect energy level (or, simply, *defect level*), would be observed in experiments where the defect in the final charge state q' fully relaxes to its equilibrium configuration after the transition.

Defect-to-band and band-to-defect optical transitions, including those of the charge-transfer type [32], can be characterized using the *optical* transition level $E_{\text{opt}}^{q/q'}$ that is defined similarly to $\epsilon(q/q')$ but with the total energy

of the final state q' calculated using the lattice configuration of the initial state q [25]. For the $5d-4f$ transitions in neutral Eu defects, we calculate the energies based on a constrained occupancy approach and Δ SCF analysis (SCF: self-consistent field), similar to that used in previous studies of RE-doped phosphors [33, 34]. In this approach, we create the excited state Eu $4f^6 5d^1$ in SrAl_2O_4 by manually emptying the highest Eu $4f$ state and filling the next state lying higher in energy.

The total-energy electronic structure calculations are based on DFT with the Heyd-Scuseria-Ernzerhof (HSE) functional [24], the projector augmented wave (PAW) method [35], and a plane-wave basis set, as implemented in the Vienna *Ab Initio* Simulation Package (VASP) [36]. Along with the CPU version, the GPU port of VASP (version 6.2.1) is also used. The Hartree-Fock mixing parameter is set to 0.33 and the screening length to the default value of 10 Å to match the experimental band gap. We use the PAW potentials in the VASP database which treat Sr $4s^2 4p^6 5s^2$, Al $3s^2 3p^1$, O $2s^2 2p^4$, Eu $5s^2 5p^6 4f^7 6s^2$, and Dy $5s^2 5p^6 4f^{10} 6s^2$ explicitly as valence electrons and the rest as core. Defects are modelled using monoclinic $2 \times 1 \times 3$ (168-atom) supercells and integrations over the Brillouin zone are performed using the Γ point, except in the constrained occupancy calculations (using VASP 5.3.3) where $1 \times 1 \times 3$ (84-atom) supercells and a Γ -centered $2 \times 2 \times 1$ k -point mesh are used. In the defect calculations, the lattice parameters are fixed to the calculated bulk values but all the internal coordinates are relaxed. In all the calculations, the plane-wave basis-set cutoff is set to 500 eV and spin polarization is included; structural relaxations are performed with the HSE functional and the force threshold is chosen to be 0.02 eV/Å. Spin-orbit interaction is not included as it has negligible effects on the defect transition levels [28].

The chemical potentials of Sr, Al, and O vary over a range determined by requiring that the host compound SrAl_2O_4 is stable against competing Sr–Al–O phases; see Sec. III A. Experimentally relevant or representative sets of μ_{Sr} , μ_{Al} , and μ_{O} are adopted to present defect formation energies. The chemical potential of Dy is obtained by assuming equilibrium with Dy_2O_3 ; that of Eu by assuming equilibrium with Eu_2O_3 (under oxidizing conditions) or EuO (under reducing conditions). It should be noted that the transition levels $\epsilon(q/q')$ and $E_{\text{opt}}^{q/q'}$ are *independent* of the choice of the atomic chemical potentials.

III. RESULTS AND DISCUSSION

A. Bulk properties

SrAl_2O_4 crystallizes in the monoclinic $P2_1$ space group [37]; see Fig. 9 in Appendix A. Its crystal structure has two inequivalent Sr lattice sites, four inequivalent Al sites, and eight inequivalent O sites. The Sr sites, Sr1 and Sr2, are in channels along the c -axis formed by the Al–O framework (hereafter referred to as the Sr1 and Sr2 chan-

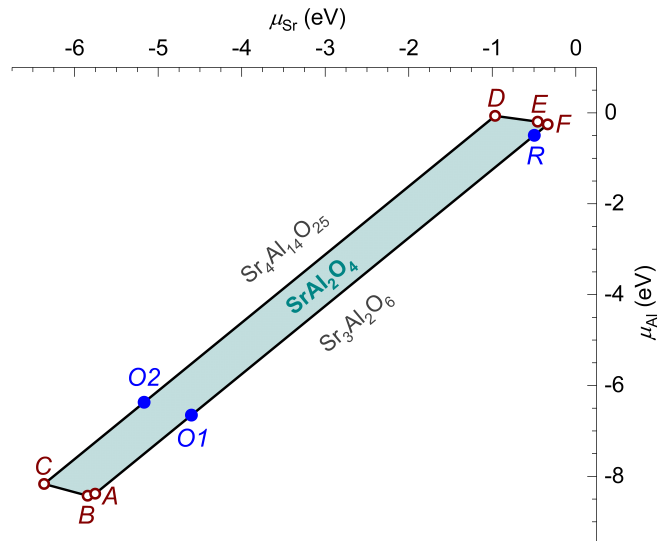


FIG. 2. Chemical-potential phase diagram for SrAl_2O_4 . Sr–Al–O phases that define the stability region of the host, shown as a shaded polygon, are SrO_2 (the AB line), O_2 (BC), $\text{Sr}_4\text{Al}_{14}\text{O}_{25}$ (CD), SrAl_4 (DE), SrAl_2 (EF), and $\text{Sr}_3\text{Al}_2\text{O}_6$ (FA). Points $O1$, $O2$, and R are examples of experimentally relevant oxidizing and reducing environments; see the text.

nels). The calculated lattice parameters are $a = 8.4491$ Å, $b = 8.8159$ Å, $c = 5.1525$ Å, and $\beta = 93.5397^\circ$, in excellent agreement with the experimental values [37]. The calculated band gap is 6.51 eV, an indirect gap with the valence-band maximum (VBM) at the X point in the Brillouin zone and the conduction-band minimum (CBM) at the Γ point. For comparison, the reported experimental band gap is 6.5–6.6 eV [5, 38, 39]. The VBM consists primarily of the O $2p$ states, whereas the CBM consists of a mixture of the Sr, Al, and O s states. The total static dielectric constant is calculated to be 9.36 (taken as the average of the xx , yy , and zz components) with the electronic contribution based on the real part of the dielectric function $\epsilon_1(\omega)$ for $\omega \rightarrow 0$ obtained within HSE and the ionic contribution calculated using density-functional perturbation theory [40] within the generalized-gradient approximation [41].

Figure 2 shows the phase stability of SrAl_2O_4 . The formation enthalpies (calculated at 0 K) of different Sr–Al–O phases are listed in Table I in Appendix A. The initial structures of these phases are taken from the Materials Project database [42]. The stability region of SrAl_2O_4 is delineated mainly by $\text{Sr}_3\text{Al}_2\text{O}_6$ and $\text{Sr}_4\text{Al}_{14}\text{O}_{25}$, which is consistent with the experimental phase diagram [43, 44].

In the presentation of defect formation energies in the next sections, we make use of the following points in the phase diagram: (i) $O1$, where the host compound is in equilibrium with $\text{Sr}_3\text{Al}_2\text{O}_6$ and air (the oxygen partial pressure $p_{\text{O}_2} = 0.21$ atm) at 750°C , (ii) $O2$, where the host is in equilibrium with $\text{Sr}_4\text{Al}_{14}\text{O}_{25}$ and air at 750°C , and (iii) R , where the host is in equilibrium with

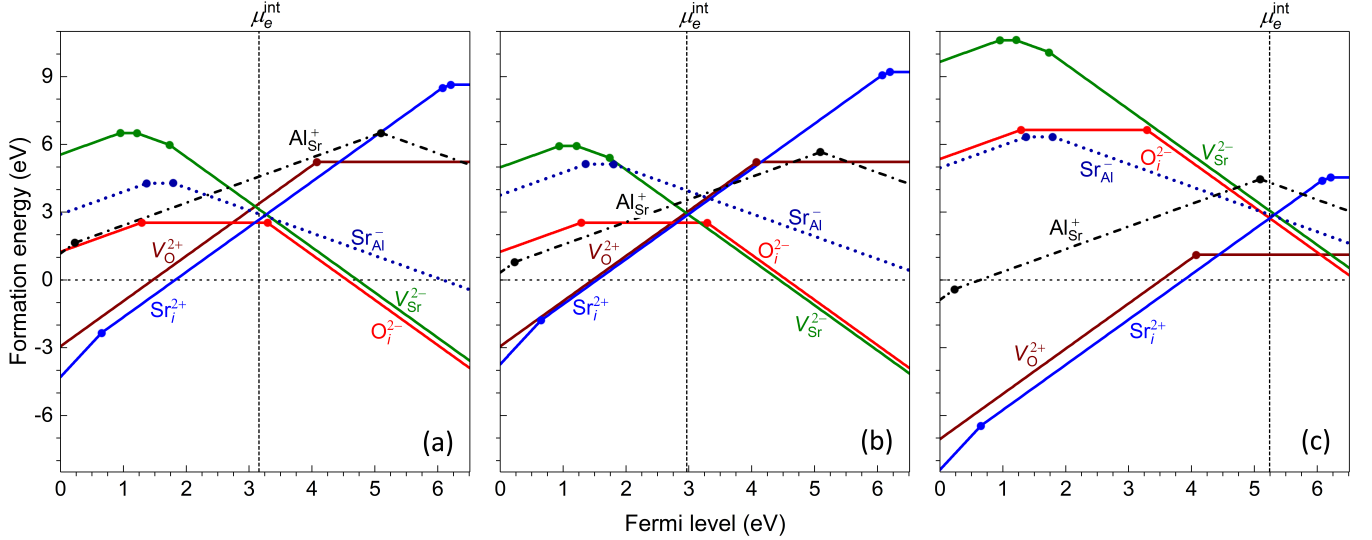


FIG. 3. Formation energies of native defects in SrAl_2O_4 , as a function of the Fermi level from the VBM (0 eV) to the CBM (6.51 eV), calculated at points (a) $O1$, (b) $O2$, and (c) R in the phase diagram (Fig. 2). For each defect, only segments of the formation energy lines corresponding to the lowest-energy charge states are shown. The slope of these segments indicates the charge state q : positively (negatively) charged defect configurations have positive (negative) slopes; horizontal segments correspond to neutral defect configurations. Large dots connecting two segments with different slopes mark the *defect levels* $\epsilon(q/q')$. For a defect with multiple inequivalent lattice sites, only the lowest-energy lattice site is reported.

$\text{Sr}_3\text{Al}_2\text{O}_6$ and Ar/H_2 5% ($p_{\text{O}_2} \sim 10^{-20}$ atm) at 1400°C . Points $O1$ and $O2$ (with $\mu_{\text{O}} = -1.20$ eV) represent oxidizing environments, whereas point R ($\mu_{\text{O}} = -5.30$ eV) represents a highly reducing environment. Here, μ_{O} is calculated as half of the Gibbs free energy of O_2 gas at the given T and p_{O_2} values [45]. These conditions are chosen to reflect the conditions under which undoped and Eu-doped SrAl_2O_4 samples are often prepared. Beauger [16] reported the presence of $\text{Sr}_3\text{Al}_2\text{O}_6$ as an impurity phase, indicating that their synthesis environment corresponds to a point very close to the FA line in Fig. 2.

B. Native point defects

Figure 3 shows the formation energy of native defects in SrAl_2O_4 . The defects introduce one or more energy levels in the host's band gap region (marked by large dots in the figure; explicit numerical values are listed in Table II). Under the experimentally relevant conditions (see Sec. III A), the dominant defects (i.e., those with the lowest formation energy) are Sr and O vacancies and interstitials. In the absence of impurities, intentionally doped or unintentionally present, the Fermi level is “pinned” at the position μ_e^{int} (“int” for intrinsic), determined predominantly by the lowest-energy charged defects, where the charge neutrality condition (3) is maintained. From one point in the phase diagram (Fig. 2) to another, the *defect landscape* in SrAl_2O_4 changes, leading to a change in the μ_e^{int} value; e.g., μ_e^{int} moves toward the CBM in going from oxidizing (points $O1$ and $O2$) to reducing (point R)

synthesis conditions. We find that μ_e^{int} varies from 2.28 eV (under the conditions at point C) to 5.36 eV (point F). The Fermi level of SrAl_2O_4 , even in the presence of intentional and/or unintentional impurities, cannot be close to the VBM (under all synthesis conditions) but can, in principle, be high up at the CBM (under reducing synthesis conditions only). This is because the formation energy of certain native defects, specifically Sr interstitials and O vacancies, is negative in the region near the VBM (up to $E_v + 0.94$ eV at point C and higher at other points in the phase diagram), whereas the native defects can all have a positive formation energy under the reducing conditions (e.g., those at points $D-F$ and R).

The removal of an O^{2-} results in a positively charged O vacancy (V_{O}^{2+} , spin $S = 0$). Other charge states, V_{O}^+ ($S = 1/2$) and V_{O}^0 ($S = 0$), are also stable. The energetics and electronic behavior of V_{O} are different at the inequivalent O lattice sites due to the slightly different local lattice environments. At certain O sites (e.g., at the $O8$ site as shown in Fig. 3), V_{O}^0 is energetically less favorable than V_{O}^{2+} and V_{O}^+ in the entire range of the Fermi-level values. Notably, the energy levels introduced by the vacancy at the $O1$ to $O8$ sites are all about 2.43–3.55 eV below the CBM; see Fig. 10. The lowest-energy V_{O}^{2+} configuration occurs at the $O8$ site, see Fig. 4(a), indicating that the Al– $O8$ bonds are weakest. The highest-energy V_{O}^{2+} occurs at the $O1$ site. Under reducing conditions (e.g., at point R), V_{O} occurs in the form of V_{O}^0 with a high concentration (highest among all native defects).

Our results for the oxygen vacancies are thus in *sharp contrast* to those of Finley et al. [47] where the defect

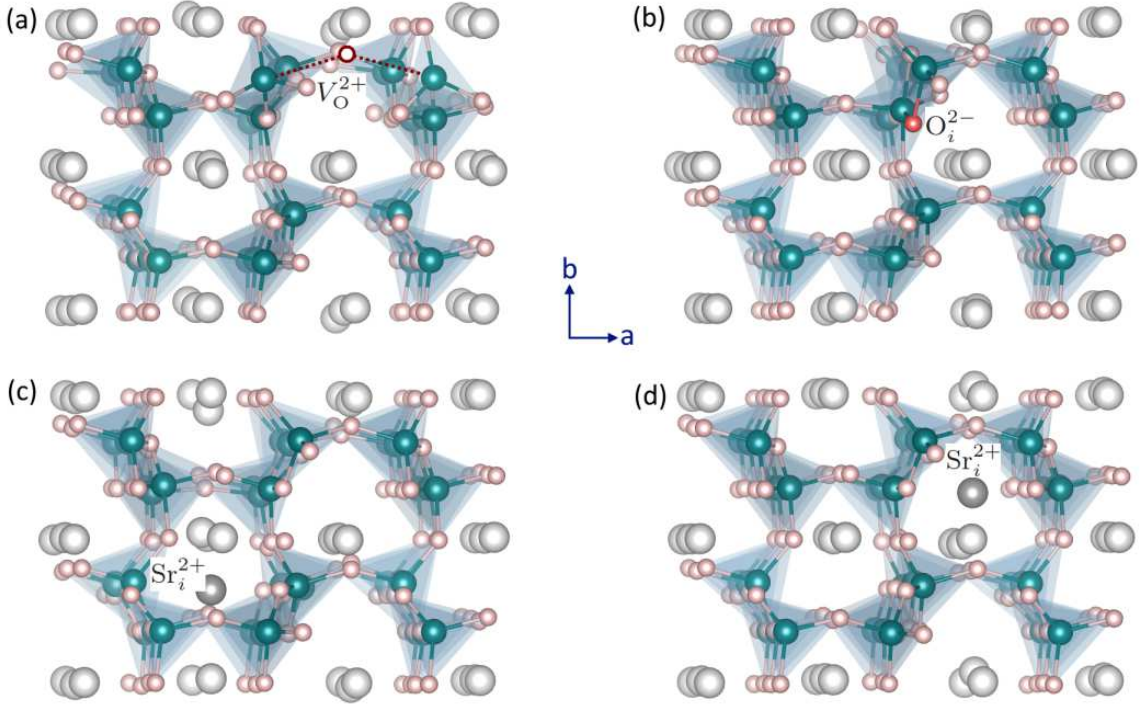


FIG. 4. Structures of selected native defect configurations in SrAl₂O₄: (a) V_{O}^{2+} at the O8 lattice site, (b) O_i^{2-} , (c) Sr_i^{2+} in the Sr1 channel, and (d) Sr_i^{2+} in the Sr2 channel. Large (gray) spheres are Sr, medium (blue) are Al, and small (red) are O. All the atomic structures in this work are visualized using the VESTA package [46].

energy levels introduced by V_{O} were found to scatter all over the upper half of the host band gap region. Given the similarity in the bonding environments of the inequivalent O sites (e.g., every single O atom is bonded to two Al atoms), the almost random distribution of the defect levels reported in Ref. [47] cannot be justified.

The addition of an oxygen, which results in an oxygen interstitial (O_i), introduces energy levels near the midgap region; see also Table II. In the O_i^{2-} ($S = 0$) configuration, the added O^{2-} is shared between two AlO_4 units; Fig. 4(b) [and Fig. 11(a)]. O_i^- ($S = 1/2$; not visible in Fig. 3 due to its very small stability range) is a complex of O_i^{2-} and an electron hole localized at an O site (hereafter referred to as η_{O}^+ , $S = 1/2$). The structure of O_i^0 [$S = 0$; Fig. 11(b)] can be described as having the interstitial oxygen bonded to one of the O atoms in an AlO_4 unit (the O–O distance is 1.48 Å), resulting in a distorted AlO_5 . O_i^+ ($S = 1/2$) is a complex of O_i^0 and η_{O}^+ .

The removal of a Sr^{2+} ion from the host lattice results in a negatively charged Sr vacancy (V_{Sr}^{2-} , $S = 0$). Other stable charge states of V_{Sr} are V_{Sr}^- ($S = 1/2$), V_{Sr}^0 ($S = 1$), and V_{Sr}^+ ($S = 3/2$), which can be regarded as complexes consisting of V_{Sr}^{2-} and one, two, and three η_{O}^+ defects, respectively. V_{Sr} at the Sr1 site is slightly lower in energy than that at the Sr2 site, e.g., by 0.08 eV in the case of V_{Sr}^{2-} . The defect levels associated with V_{Sr} are in the lower half of the band gap region; see also Table II.

There are two possible sites for Sr interstitials (Sr_i):

one, Sr_{i1} , locating in the Sr1 channel (along the c -axis) but off the Sr1 chain and between two Al atoms (along the a -axis), see Fig. 4(c), and the other, Sr_{i2} , in the Sr2 channel but off the Sr2 chain and between two Al atoms (along the a -axis), see Fig. 4(d) [and Fig. 11(c)]. Sr_{i1} and Sr_{i2} are approximately at the interstitial sites V2 and V1, respectively, mentioned in Bierwagen et al. [14]. Sr_{i2} is lower in energy than Sr_{i1} (e.g., by 0.19 eV in the case of Sr_i^{2+} , $S = 0$). The defect introduces three defect levels: one above the VBM and two just below the CBM. The other charge states are Sr_i^{3+} ($S = 1/2$; a complex of Sr_i^{2+} and η_{O}^+), Sr_i^+ ($S = 1/2$), and Sr_i^0 ($S = 0$). At μ_e^{int} , Sr_i^{2+} is energetically most stable among the stable charge states of Sr_i and one of the lowest-energy native defects.

Antisite defects, Al_{Sr} and Sr_{Al} , are also considered. We find that they are higher in energy than the Sr and O vacancies and interstitials. Al_{Sr} is lower in energy at the Sr2 site than at the Sr1 site, e.g., 0.55 eV lower in the case of Al_{Sr}^+ ($S = 0$); $\text{Al}_{\text{Sr}}^{2+}$ ($S = 1/2$) is a complex of Al_{Sr}^+ and η_{O}^+ . Sr_{Al} is energetically most favorable at the Al2 site; Sr_{Al}^0 ($S = 1/2$) and Sr_{Al}^+ ($S = 1$) are defect complexes of Sr_{Al}^- and one and two η_{O}^+ , respectively. Finally, the creation of Al vacancies (V_{Al}) involves breaking four strongly covalent Al–O bonds, a high energy process. Such defects, as well as Al interstitials (Al_i), have high formation energies and are thus not included here.

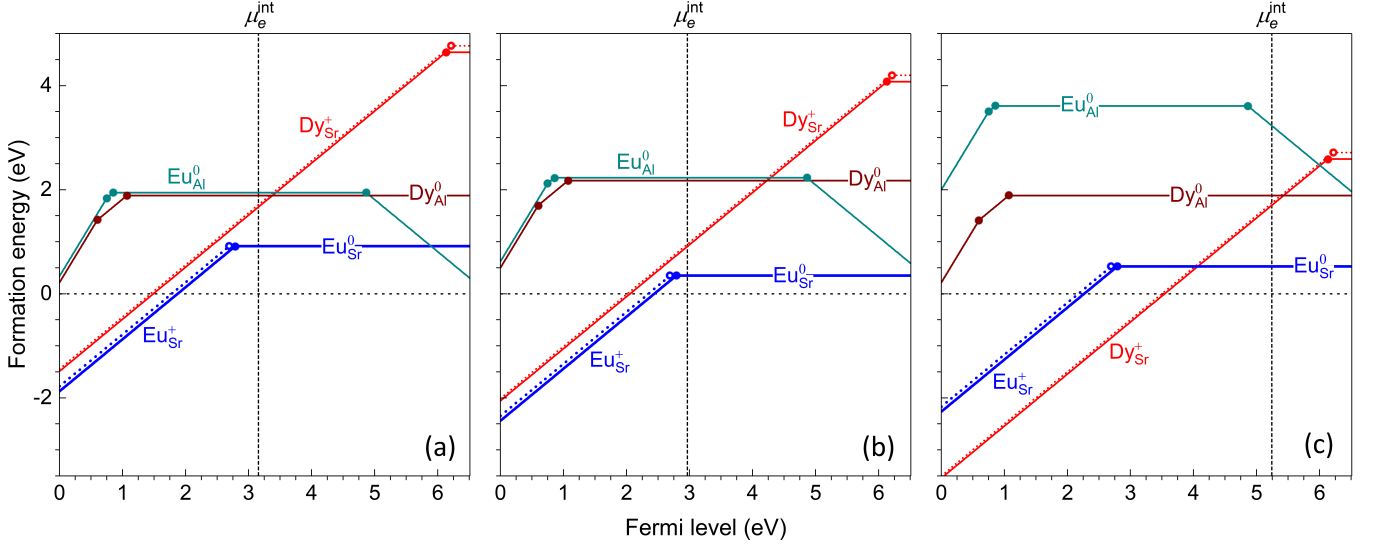


FIG. 5. Formation energies of Eu- and Dy-related defects in SrAl_2O_4 , calculated at points (a) O1, (b) O2, and (c) R in the phase diagram (Fig. 2). Large dots connecting two segments with different slopes mark the *defect levels*. For Eu_{Sr} and Dy_{Sr} , the defect configurations at both the Sr1 (dotted lines) and Sr2 (solid lines) sites are included.

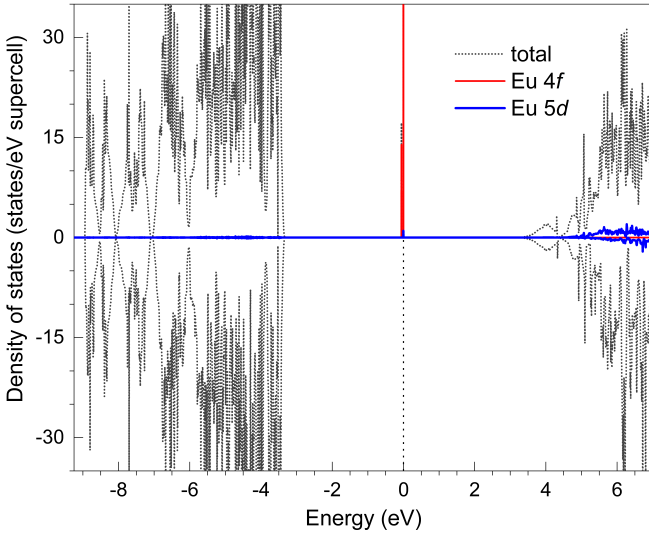


FIG. 6. Total and projected densities of states of Eu-doped SrAl_2O_4 , specifically the Eu_{Sr}^0 defect configuration with the chemical composition $\text{Eu}_x\text{Sr}_{1-x}\text{Al}_2\text{O}_4$ ($x = 0.125$). The zero of energy is set to the highest occupied state.

C. Rare-earth (co)dopants

Figure 5 shows the formation energy of substitutional Eu and Dy impurities at the Sr and Al sites. Results for the REs at the interstitial sites are included in Fig. 12. Table II lists explicit numerical values of the energy levels and stable RE ions. We find that, at and near the Fermi level determined by the native defects (μ_e^{int}), RE_{Sr} is lower in energy than RE_{Al} and RE_i , indicating that Eu and Dy are incorporated into SrAl_2O_4 at the Sr sites.

Eu_{Sr} is stable as Eu_{Sr}^0 (i.e., Eu^{2+} , with a magnetic moment of $7\mu_B$; spin $S = 7/2$) and/or Eu_{Sr}^+ (i.e., Eu^{3+} , with a magnetic moment of $6\mu_B$; $S = 3$). The Eu_{Sr}^0 configurations at the Sr1 and Sr2 sites are almost degenerate in energy, whereas Eu_{Sr}^+ at the Sr2 site is 0.09 eV lower in energy than at the Sr1 site. The (+/0) level of Eu_{Sr} is 2.69 eV above the VBM when incorporated at the Sr1 site or 2.79 eV when incorporated at the Sr2 site; below (above) this level, Eu^{3+} (Eu^{2+}) is energetically more favorable. The $\text{Eu}^{2+}/\text{Eu}^{3+}$ ratio thus depends on the actual position of the Fermi level which, in turn, depends on the synthesis conditions. The ratio is high under reducing conditions (e.g., at point R) and decreases as one changes from reducing to oxidizing conditions. Note that, under actual synthesis conditions and as Eu-doped SrAl_2O_4 is typically prepared using Eu^{3+} as dopant, an equilibrium assumption may not hold true, and the trivalent ion may be frozen in [14]. In other words, Eu^{3+} may be present even in samples prepared under less oxidizing conditions.

The mixed valence of Eu in SrAl_2O_4 can be understood based on the calculated electronic structure of Eu_{Sr}^0 , reported in Fig. 6. The HSE calculations of the electronic density of states are carried out using a smaller, $1 \times 1 \times 2$ supercell and a Γ -centered $3 \times 3 \times 3$ k -point mesh. Eu_{Sr}^0 has seven occupied spin-up 4f states in the host band gap (and seven spin-down unoccupied 4f states deep in the conduction band). Given the electronic structure, when one electron is removed from this neutral defect configuration, the electron is removed from the highest occupied state (which is the highest Eu 4f state). This results in the divalent Eu^{2+} ($4f^7$) being oxidized to the trivalent Eu^{3+} ($4f^6$), i.e., Eu_{Sr}^0 to Eu_{Sr}^+ . Figure 13(a) shows the localized Eu 4f electron associated with Eu_{Sr}^0 .

At and near μ_e^{int} , Eu_{Al} is stable as Eu_{Al}^0 (i.e., Eu^{3+})

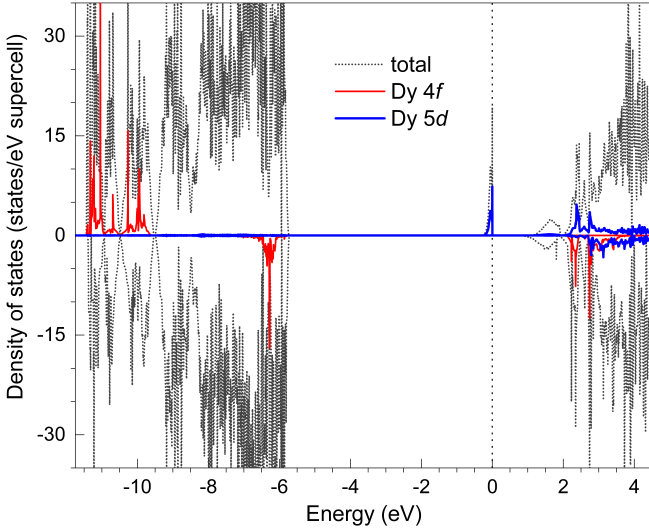


FIG. 7. Total and projected densities of states of Dy-doped SrAl_2O_4 , specifically the Dy_{Sr}^0 defect configuration with the chemical composition $\text{Dy}_x\text{Sr}_{1-x}\text{Al}_2\text{O}_4$ ($x = 0.125$). The zero of energy is set to the highest occupied state.

under the oxidizing conditions (O1 and O2), and as Eu_{Al}^- (i.e., Eu^{2+}) and/or Eu_{Al}^0 under the reducing condition (R). Other electronically stable charge states are Eu_{Al}^+ (a complex of Eu_{Al}^0 and η_{O}^+) and $\text{Eu}_{\text{Al}}^{2+}$ (a complex of Eu_{Al}^0 and two η_{O}^+). These positively charged states, however, cannot be obtained during synthesis due to the negative formation energies of Eu_{Sr} and the native defects in the region above the VBM. We find that, at and near μ_e^{int} , Eu_i is electronically stable as Eu_i^{2+} (i.e., Eu^{2+}) and has a much higher formation energy than Eu_{Sr} and Eu_{Al} .

The mixed valence of Eu is well discussed in the experimental literature [14, 16, 19, 48]. The fact that both Eu^{3+} and Eu^{2+} can be realized in as-prepared SrAl_2O_4 is consistent with the above results showing the (+/0) level of Eu_{Sr} is located near midgap and the stability ranges of Eu_{Sr}^+ and Eu_{Sr}^0 are accessible during synthesis. Wang et al. [49] found Eu^{2+} to be distributed almost equally at the two Sr sites, consistent with the fact that the energies of Eu_{Sr}^0 at the Sr1 and Sr2 sites are almost equal. Note that other valence states of Eu (e.g., Eu^+ , as proposed by Matsuzawa et al. [5]) cannot be stabilized electronically.

Dy_{Sr} is energetically favorable as Dy_{Sr}^+ (i.e., Dy^{3+} ; $S = 5/2$) in almost the entire range of the Fermi-level values and as Dy_{Sr}^0 (i.e., Dy^{2+} ; $S = 3$) in a small range below the CBM. The (+/0) level is located at 6.21 eV (6.13 eV) above the VBM, i.e., 0.30 eV (0.38 eV) from the CBM, at the Sr1 (Sr2) site. The defect is slightly lower in energy at the Sr2 site than at the Sr1 site; the difference is 0.12 eV for Dy_{Sr}^0 or 0.05 eV for Dy_{Sr}^+ . We find that the electronic configuration of Dy^{3+} is $4f^9$, whereas that of Dy^{2+} is $4f^9 5d^1$. Figure 7 shows the electronic structure of Dy_{Sr}^0 . The nine (seven spin-up and two spin-down) occupied Dy 4f states are in the valence band, the occupied Dy 5d¹ state is in the upper half of the host band gap, and

the five spin-down unoccupied Dy 4f states are in the conduction band. When one electron is removed from Dy_{Sr}^0 , it is removed from the Dy 5d¹ state, which leads to the formation of Dy_{Sr}^+ . Figure 13(c) shows the localized Dy 5d electron associated with the Dy_{Sr}^0 configuration.

Dy_{Al} is stable as Dy_{Al}^0 (i.e., Dy^{3+}), except near the VBM where it is stable as Dy_{Al}^+ (i.e., Dy^{4+} with the electronic configuration $4f^8$) or $\text{Dy}_{\text{Al}}^{2+}$ (a complex of Dy_{Al}^+ and η_{O}^+). However, given the negative formation energy of Dy_{Sr} and the native defects in the region above the VBM, these positive charge states are inaccessible during synthesis. Dy_i is stable as Dy_i^{3+} ; see Fig. 12. At and near μ_e^{int} , Dy_{Al} and Dy_i are all higher energy than Dy_{Sr} , indicating that Dy is incorporated at the Sr sites.

The results for the Dy-related defects thus confirm the stabilization of Dy_{Sr}^+ , consistent with the fact that Dy is present as Dy^{3+} in as-prepared Dy-doped samples. Interestingly, Dy_{Sr}^0 (i.e., Dy^{2+}) is also found to be structurally and electronically stable. Dy_{Sr}^0 , however, has a very small stability range that is close to the CBM, and in that range Dy_{Sr} becomes much less favorable energetically than Dy_{Al}^0 (i.e., Dy^{3+}), indicating that the divalent Dy^{2+} is almost impossible to obtain during synthesis. It can be photogenerated under irradiation nonetheless. Experimentally, Joos et al. [50] reported evidence of the $\text{Dy}^{3+/2+}$ valence change in (Eu, Dy)-doped $\text{Sr}_4\text{Al}_{14}\text{O}_{25}$ under laser excitation. A similar process for Dy could be observed in SrAl_2O_4 . Note that Dorenbos [20] estimated the “ground state of Dy^{2+} ” to be at 0.9 eV below the CBM, based on a semiempirical model. Such a level is much lower than our calculated (+/0) level of Dy_{Sr} . Our results also show that Dy^{4+} is not stable electronically at the Sr site; the tetravalent ion is stable at the Al site but energetically unfavorable, as discussed above.

Finally, we consider possible association between Eu_{Sr} and Dy_{Sr} or a native defect. Figure 14 shows the formation energy of $\text{Eu}_{\text{Sr}}\text{-Dy}_{\text{Sr}}$, $\text{Eu}_{\text{Sr}}\text{-V}_{\text{O}}$, $\text{Eu}_{\text{Sr}}\text{-O}_i$, $\text{Eu}_{\text{Sr}}\text{-V}_{\text{Sr}}$, and $\text{Eu}_{\text{Sr}}\text{-Sr}_i$; see also Table III for details on the stable charge states of the complexes. Focusing on the Fermi-level range near the CBM, which is relevant to the physics under investigation, we find that the electronic behavior of the complexes is determined predominantly by the non-Eu constituent. Specifically, $(\text{Eu}_{\text{Sr}}\text{-Dy}_{\text{Sr}})^+$ is a defect complex consisting of Eu_{Sr}^0 and Dy_{Sr}^+ and $(\text{Eu}_{\text{Sr}}\text{-Dy}_{\text{Sr}})^0$ is a complex of Eu_{Sr}^0 and Dy_{Sr}^0 ; $(\text{Eu}_{\text{Sr}}\text{-V}_{\text{O}})^0$ is a complex of Eu_{Sr}^0 and V_{O}^0 ; $(\text{Eu}_{\text{Sr}}\text{-O}_i)^{2-}$ is a complex of Eu_{Sr}^0 and O_i^{2-} ; $(\text{Eu}_{\text{Sr}}\text{-V}_{\text{Sr}})^{2-}$ is a complex of Eu_{Sr}^0 and $\text{V}_{\text{Sr}}^{2-}$; $(\text{Eu}_{\text{Sr}}\text{-Sr}_i)^{2+}$ is a complex of Eu_{Sr}^0 and Sr_i^{2+} , $(\text{Eu}_{\text{Sr}}\text{-Sr}_i)^+$ is a complex of Eu_{Sr}^0 and Sr_i^+ , and $(\text{Eu}_{\text{Sr}}\text{-Sr}_i)^0$ is a complex of Eu_{Sr}^0 and Sr_i^0 . Note that we determine the charge state of a defect configuration by examining the calculated total and local magnetic moments, electron occupation, and local lattice environment. The (+/0) level of $\text{Eu}_{\text{Sr}}\text{-Dy}_{\text{Sr}}$ is 6.11 eV above the VBM, almost the same as that of the isolated Dy_{Sr} ; the (2+/+) and (+/0) levels of $\text{Eu}_{\text{Sr}}\text{-Sr}_i$ are 6.04 eV and 6.21 eV above the VBM, almost the same as those of the isolated Sr_i .

Most notably, we find that the binding energy of the

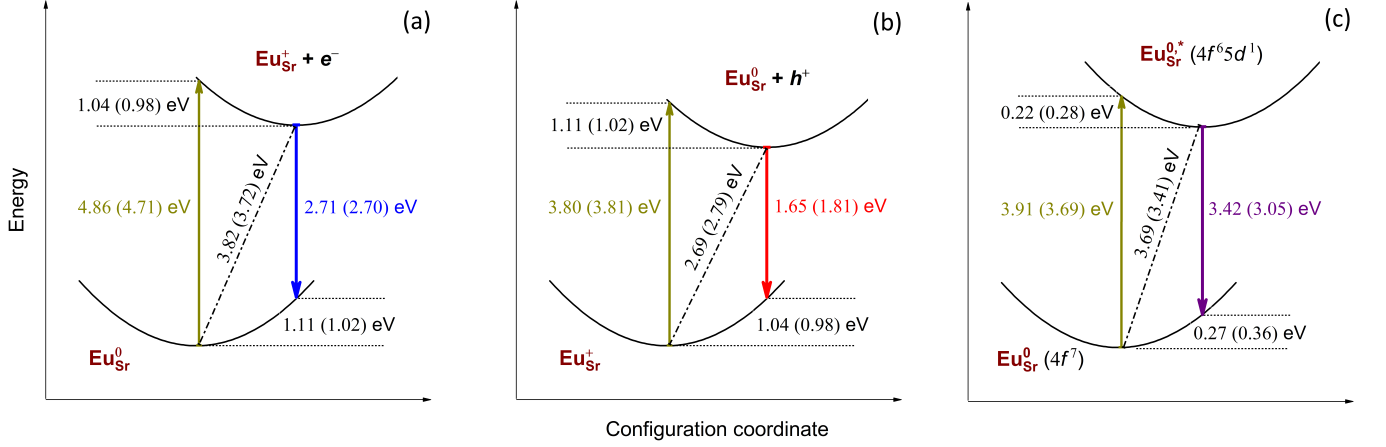


FIG. 8. Configuration-coordinate diagram illustrating optical absorption (up arrow) and emission (down arrow) processes for Eu_{Sr} in SrAl_2O_4 : band-defect transitions involving the $(+ / 0)$ defect level of Eu_{Sr} exchanging (a) electrons with the CBM or (b) holes with the VBM, and (c) interconfigurational $5d-4f$ transitions in $\text{Eu}_{\text{Sr}}^{0+}$. The dash-dotted line indicates the thermal energy (i.e., ZPL). The values sandwiched between two dotted lines are the relaxation energies (i.e., the Franck-Condon shifts). The values outside (inside) the brackets are for Eu at the Sr1 (Sr2) lattice site. Axes are not to scale.

Eu-related complexes is very small or even negative, see Table III, indicating that they are not stable under thermodynamic equilibrium, which is also consistent with the above analysis of the electronic behavior. In other words, Eu_{Sr} is unlikely to stay close and form a defect complex with Dy_{Sr} or any of the dominant native defects in SrAl_2O_4 , and even if it does, e.g., when the constituent defects get trapped next to each other, the electronic behavior of the complex in the relevant range of Fermi-level values is not that different from the isolated constituents. Our results for $\text{Eu}_{\text{Sr}}\text{-Dy}_{\text{Sr}}$ are thus consistent with experimental observations that, in $(\text{Eu}^{2+}, \text{RE}^{3+})$ -doped SrAl_2O_4 , the RE^{3+} co-dopant only enhances the afterglow time and intensity and does not change the position or the shape of the emission band [5, 51].

D. Eu-related optical transitions

Let us now examine possible band-defect and interconfigurational $5d-4f$ optical transitions involving the Eu_{Sr} defect (The intraconfigurational Eu $4f-4f$ optical transitions are not explicitly considered in this work).

Figure 8(a) illustrates the optical absorption (defect-to-band) and emission (band-to-defect) processes involving the $(+ / 0)$ level of Eu_{Sr} exchanging electrons with the CBM. Under illumination, for example, the Eu_{Sr}^0 configuration (e.g., present in as-prepared Eu-doped SrAl_2O_4 samples) can absorb a photon and become ionized to Eu_{Sr}^+ with the removed electron being excited into the conduction band. The peak absorption energy (E_{abs}) related to the optical transition level $E_{\text{opt}}^{0/+}$ (the formation energy difference between Eu_{Sr}^0 and the Eu_{Sr}^+ configuration in the lattice geometry of Eu_{Sr}^0) is 4.86 eV (4.71 eV), with a relaxation energy (i.e., the Franck-Condon shift, d_{FC}^e)

of 1.04 eV (0.98 eV), when Eu is incorporated at the Sr1 (Sr2) lattice site. With such a large relaxation energy, the emission is expected to be broad. In the reverse process, Eu_{Sr}^+ can capture an electron from the CBM, e.g., previously excited from Eu_{Sr}^0 (or from the valence band) to the conduction band. If the recombination is *radiative*, a photon will be emitted. The peak emission energy (E_{em}) related to the optical transition level $E_{\text{opt}}^{+/0}$ (the formation energy difference between Eu_{Sr}^+ and the Eu_{Sr}^0 configuration in the lattice geometry of Eu_{Sr}^+) is 2.71 eV (2.70 eV), with a relaxation energy (d_{FC}^e) of 1.11 eV (1.02 eV), at the Sr1 (Sr2) site. The thermal energy (E_{therm} ; also referred to as the zero-phonon line or ZPL) associated with the $\text{Eu}_{\text{Sr}}^0 \rightleftharpoons \text{Eu}_{\text{Sr}}^+ + e^-$ transitions is 3.38 eV (3.25 eV) at the Sr1 (Sr2) site, measured from the CBM. The ZPL marks the initial *onset* of the absorption band.

Note, however, that the band-to-defect emission process $\text{Eu}_{\text{Sr}}^+ + e^- \rightarrow \text{Eu}_{\text{Sr}}^0$ may not occur at all due to another, competing process in which the recombination is *nonradiatively*: $\text{Eu}_{\text{Sr}}^+ + e^- \rightarrow \text{Eu}_{\text{Sr}}^{0,*}$, where $\text{Eu}_{\text{Sr}}^{0,*}$ is Eu^{2+} in its excited state $4f^6 5d^1$. In this case, $\text{Eu}_{\text{Sr}}^{0,*}$ will relax to its ground state Eu_{Sr}^0 and release a photon through the allowed $5d-4f$ transition (discussed below).

In addition to exchanging electrons with the CBM, the $(+ / 0)$ level of Eu_{Sr} can also exchange holes with the VBM. Figure 8(b) illustrates the absorption and emission $\text{Eu}_{\text{Sr}}^0 \rightleftharpoons \text{Eu}_{\text{Sr}}^0 + h^+$ processes. In the literature, these processes are often regarded as involving an O^{2-} to Eu^{3+} charge transfer (CT) and referred to as CT processes [13, 19]. The hole (h^+) state at the VBM consists primarily of the O $2p$ states, as discussed earlier. Our calculations show a different set of the absorption, emission, relaxation, and thermal energies as indicated in Fig. 8(b). Similar to the earlier case, the band-to-defect emission $\text{Eu}_{\text{Sr}}^0 + h^+ \rightarrow \text{Eu}_{\text{Sr}}^+$ may not be observed. This

is because the energy from the recombination of the electron localized at Eu_{Sr}^0 and the free hole can quickly be absorbed into the $4f$ -electron core of Eu^{3+} which then excites the ion and leads to intra- f luminescence, as previously discussed in the case of RE-doped GaN [52].

Experimentally, Botterman et al. [15] reported a broad excitation band peaking at 276 nm (4.49 eV); Zollfrank et al. [13] and Bierwagen et al. [14] reported a similar value, at 250 nm (4.96 eV). This band has often been assigned to an O^{2-} to Eu^{3+} charge transfer [13], which corresponds to the $\text{Eu}_{\text{Sr}}^+ \rightarrow \text{Eu}_{\text{Sr}}^0 + h^+$ process [$E_{\text{abs}} = 3.80$ or 3.81 eV; Fig. 8(b)] in our work. On the basis of our results, however, that excitation band should *instead* be assigned to the $\text{Eu}_{\text{Sr}}^0 \rightarrow \text{Eu}_{\text{Sr}}^+ + e^-$ process [$E_{\text{abs}} = 4.86$ or 4.71 eV; Fig. 8(a)]. Note that there have been no reports of broad CT emission bands; and only sharp $4f$ – $4f$ transitions are observed in the emission spectrum of Eu^{3+} in SrAl_2O_4 [14, 15]. This appears to be consistent with our discussion regarding alternative emission processes.

Figure 8(c) illustrates similar processes, but now involving the electric-dipole allowed $5d$ – $4f$ transitions in the neutral defect configuration Eu_{Sr}^0 and with the energies obtained from constrained occupancy HSE calculations. In the absorption process, Eu_{Sr}^0 ($4f^7$) absorbs a photon and becomes $\text{Eu}_{\text{Sr}}^{0,*}$ ($4f^65d^1$) with an electron being excited to a higher lying level which is the lowest Eu $5d^1$ state (that is now pushed down from the conduction band due to the occupation of the excited electron). The peak absorption energy related to the $4f^7 \rightarrow 4f^65d^1$, i.e., the total-energy difference between Eu_{Sr}^0 ($4f^7$) and the excited configuration $\text{Eu}_{\text{Sr}}^{0,*}$ ($4f^65d^1$) in the lattice geometry of the former, is 3.91 eV (3.69 eV), with a relaxation energy $d_{\text{FC}}^e = 0.22$ eV (0.28 eV), when Eu is incorporated at the Sr1 (Sr2) site. The ZPL, 3.69 eV (3.41 eV) at the Sr1 (Sr2) site, is the total-energy difference between the ground state $4f^7$ [Fig. 13(a)] and the excited state $4f^65d^1$ [Fig. 13(b)]. In the reverse process, the excited electron recombines radiatively with the hole that has been left behind and emits a photon. The peak emission energy related to the $4f^65d^1 \rightarrow 4f^7$ process, i.e., the total-energy difference between the excited $\text{Eu}_{\text{Sr}}^{0,*}$ ($4f^65d^1$) and the ground state Eu_{Sr}^0 ($4f^7$) in the lattice geometry of the former, is 3.42 eV (3.05 eV), with a relaxation energy $d_{\text{FC}}^g = 0.27$ eV (0.36 eV), when Eu is at the Sr1 (Sr2) site. The Stokes shift, $\Delta S = d_{\text{FC}}^e + d_{\text{FC}}^g$, is calculated to be 0.49 (0.64) eV at the Sr1 (Sr2) site.

Although there are differences between our calculated energies for the $4f^7 \rightleftharpoons 4f^65d^1$ processes (summarized in Table IV) and those obtained in experiments, the emissions at the Sr1 and Sr2 lattice sites can be identified with the two broad emission bands peaking at 445 nm (2.79 eV, blue) and 520 nm (2.38 eV, green) and the Stokes shifts of roughly 3000 cm^{-1} (0.37 eV) and 4000 cm^{-1} (0.50 eV), respectively, observed in Eu^{2+} -doped SrAl_2O_4 [12, 15, 53]. We find that the difference between the two emission energies is 0.37 eV, just like in experiments (which is larger than that for the band-defect optical transitions discussed earlier, thus indicating the $5d$ – $4f$

transitions are more sensitive to the local lattice environments). The calculated peak emission energy and Stokes shift are higher than the reported experimental values by 0.63 eV (0.67 eV) and 0.12 eV (0.14 eV) at the Sr1 (Sr2) site, respectively, which is an almost constant shift among the two lattice sites. The discrepancies with experiments may be ascribed to the electron–hole interaction that is not included in the constrained occupancy approach we employ to describe the excited state of Eu^{2+} .

Note that, using constrained occupancy DFT+ U calculations, Jia et al. [34] reported much lower values for the emission energies. For example, they obtained 2.316 (2.547) eV at the Sr1 (Sr2) site and assigned the experimentally observed green and blue luminescence bands to the Sr1 and Sr2 sites, respectively, which is different from our assignment and that of Ning et al. [54] based on multiconfigurational and constrained occupancy calculations. Our attempts to reproduce the results of Jia et al. [34] using a similar computational setup are not successful. Specifically, in our calculations based on DFT+ U [55] with $U = 7.5$ eV applied on the Eu $4f$ states, a $1 \times 1 \times 2$ (56-atom) supercell, and a $3 \times 3 \times 3$ k -point mesh, we find the emission energy is 3.52 (3.38) eV at the Sr1 (Sr2) site, which shows the same trend as in our HSE-based calculations discussed earlier; see also Table IV.

E. Carrier traps for persistent luminescence

Let us now identify charge carrier traps that can play a role in the persistent luminescence of Eu^{2+} -doped SrAl_2O_4 . Among the native point defects, we find that Sr_i can act as a trapping center for electrons. Being stable as Sr_i^{2+} in as-prepared SrAl_2O_4 , the defect can capture up to two electrons. The thermodynamic transition levels ($2 + /+$) and $(+ / 0)$ of Sr_i , at 0.44 eV and 0.30 eV below the CBM, respectively, are sufficient close to the CBM, and the positively charged carrier-capturing configurations, i.e., Sr_i^{2+} and Sr_i^+ , are electrostatically attractive to electrons from the conduction band.

Note that, in general, the carrier capture cross section increases by orders of magnitude in going from Coulomb repulsive defect centers to neutral centers to attractive centers [56]. Also note that the error bar in our calculations of the transitions levels, $\epsilon(q/q')$ and $E_{\text{opt}}^{q/q'}$, is about 0.1 eV. A discrepancy of about 0.2 eV should be expected in a comparison between the calculated and the experimental values *when* the energy levels are measured from the CBM; here, the additional 0.1 eV is to take into account a possible difference between the calculated and the actual band gaps and/or measurement uncertainties.

The presence of the Sr_i -related trapping centers can explain why the emission observed in Eu^{2+} -doped SrAl_2O_4 is persistent (albeit with a short afterglow time) even without Dy^{3+} co-doping [5, 11, 57, 58]. Notably, our results indicate that oxygen vacancies cannot act as efficient electron traps for room-temperature persistent luminescence (even when they occur with a high concentra-

tion, e.g., in samples prepared under reducing conditions) as their defect levels are too deep in the host band gap.

Finally, with the (+/0) level located at 0.30 (0.38) eV below the CBM at the Sr1 (Sr2) site as reported earlier, Dy_{Sr} can be an efficient electron trap. The electron-capturing configuration, Dy_{Sr}^+ , is positively charged. Note that, unlike Sr_i where the defect state associated with Sr_i^+ and Sr_i^0 (i.e., Sr_i^{2+} after capturing one and two electrons, respectively) is derived largely from the host states at the CBM and delocalized over several lattice sites, that associated with Dy_{Sr}^0 (i.e., Dy_{Sr}^+ after capturing an electron) is highly localized Dy $5d$ states. This indicates that the Dy_{Sr} -related traps are much more stable than the Sr_i -related ones, which is consistent with the fact that the performance of the afterglow in Eu^{2+} -doped SrAl_2O_4 is significantly improved by Dy co-doping [51, 58, 59]. First-principles calculations of photoionization and carrier capture rates [60, 61] can provide a more quantitative understanding. Also note that the presence of the (Sr_i and Dy_{Sr} related) electron traps is consistent with the fact that the $\text{Eu}^{2+} 4f^6 5d^1 \rightarrow 4f^7$ emission was observed to be quenched via the conduction band [62].

IV. CONCLUSIONS

We have carried out a comprehensive study of native point defects and rare-earth (co)dopants in SrAl_2O_4 . The major conclusions can be summarized as follows:

1. Eu is mixed valence of Eu^{2+} and Eu^{3+} and energetically most favorable at the Sr sites. The $\text{Eu}^{2+}/\text{Eu}^{3+}$ ratio can be tuned by tuning the synthesis conditions. Similarly, both Dy^{2+} and Dy^{3+} can be stabilized and are energetically most favorable at the Sr sites. Dy^{2+} is, however, always energetically much less favorable than Dy^{3+} and thus would not be realized in synthesis, although it can be photogenerated under irradiation.
2. Band-defect and interconfigurational $5d-4f$ optical transitions involving the Eu_{Sr} defect are investigated using first-principles defect calculations and a constrained occupancy approach, and alternative processes are discussed. On the basis of our results, we assign the broad blue (445 nm) and green (520 nm) emission bands observed in Eu^{2+} -doped SrAl_2O_4 to the $\text{Eu}^{2+} 4f^6 5d^1 \rightarrow 4f^7$ transition at the Sr1 and Sr2 sites, respectively.
3. Strontium interstitials are found to be efficient electron traps for room-temperature persistent luminescence. When the material is co-doped with Dy, the co-dopant

provides an even more stable electron trapping center due to the stabilization of Dy^{2+} which can explain the significantly improved performance of the afterglow in (Eu,Dy)-doped samples. Oxygen vacancies cannot be efficient electron traps, in contrast to what is commonly believed, due to their very deep defect levels.

Our work thus calls for a re-assessment of certain assumptions regarding specific defects previously made in all the mechanisms proposed for the persistent luminescence observed in Eu- and (Eu,Dy)-doped SrAl_2O_4 . It also shows a need to go beyond a constrained occupancy approach in order to obtain more quantitative results for the interconfigurational $5d-4f$ optical transitions.

ACKNOWLEDGMENTS

The author gratefully acknowledges Stéphane Jobic (Nantes Université, CNRS) for helpful discussion. This work used resources of the Center for Computationally Assisted Science and Technology (CCASt) at North Dakota State University, which were made possible in part by NSF MRI Award No. 2019077.

Appendix A: Supporting figures and tables

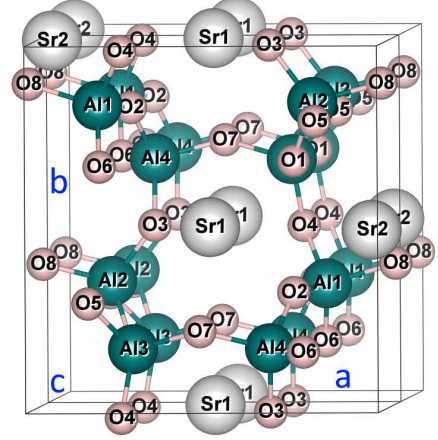


FIG. 9. Crystal structure of monoclinic SrAl_2O_4 (space group $P2_1$). The unit cell is doubled along the c -axis to show the Sr1 and Sr2 channels. Large (gray) spheres are Sr, medium (blue) are Al, and small (red) are O.

[1] P. F. Smet, K. Van den Eeckhout, O. Q. De Clercq, and D. Poelman, Persistent phosphors, in *Handbook on the Physics and Chemistry of Rare Earths*, Handbook on the Physics and Chemistry of Rare Earths, Vol. 48, edited by J.-C. Bünzli and V. K. Pecharsky (Elsevier, 2015) pp. 1–108.

[2] J. Xu and S. Tanabe, Persistent luminescence instead of phosphorescence: History, mechanism, and perspective, *J. Lumin.* **205**, 581 (2019).
 [3] D. Poelman, D. Van der Heggen, J. Du, E. Cosaert, and P. F. Smet, Persistent phosphors for the future: Fit for the right application, *J. Appl. Phys.* **128**, 240903 (2020).

- [4] Y. Murayam, N. Takeuchi, Y. Aoki, and T. Matsuzawa, Phosphorescent phosphor (1994), EP0622440.
- [5] T. Matsuzawa, Y. Aoki, N. Takeuchi, and Y. Murayama, A New Long Phosphorescent Phosphor with High Brightness, $\text{SrAl}_2\text{O}_4\text{:Eu}^{2+}, \text{Dy}^{3+}$, J. Electrochem. Soc. **143**, 2670 (1996).
- [6] R. E. Rojas-Hernandez, F. Rubio-Marcos, M. Ángel Rodríguez, and J. F. Fernandez, Long lasting phosphors: $\text{SrAl}_2\text{O}_4\text{:Eu,Dy}$ as the most studied material, Renew. Sustain. Energy Rev. **81**, 2759 (2018).
- [7] V. Vitola, D. Millers, I. Bite, K. Smits, and A. Spustaka, Recent progress in understanding the persistent luminescence in $\text{SrAl}_2\text{O}_4\text{:Eu,Dy}$, Mater. Sci. Tech. **35**, 1661 (2019).
- [8] H. H.-R. Hagemann and J. Afshani, Synthesis, luminescence and persistent luminescence of europium-doped strontium aluminates, in *Handbook on the Physics and Chemistry of Rare Earths*, Handbook on the Physics and Chemistry of Rare Earths, Vol. 60, edited by J.-C. G. Bünzli and V. K. Pecharsky (Elsevier, 2021) pp. 163–225.
- [9] F. C. Palilla, A. K. Levine, and M. R. Tomkus, Fluorescent Properties of Alkaline Earth Aluminates of the Type MAl_2O_4 Activated by Divalent Europium, J. Electrochem. Soc. **115**, 642 (1968).
- [10] G. Blasse and A. Bril, Fluorescence of Eu^{2+} -activated alkaline-earth aluminates, Philips Res. Rep. **23**, 201 (1968).
- [11] V. Abbruscato, Optical and Electrical Properties of $\text{SrAl}_2\text{O}_4\text{:Eu}^{2+}$, J. Electrochem. Soc. **118**, 930 (1971).
- [12] S. H. M. Poort, W. P. Blokpoel, and G. Blasse, Luminescence of Eu^{2+} in barium and strontium aluminate and gallate, Chem. Mater. **7**, 1547 (1995).
- [13] C. Zollfrank, S. Gruber, M. Batentschuk, A. Osvet, F. Goetz-Neunhoffer, S. Dittrich, J. Grabow, H.-D. Kurland, and F. Müller, Synthesis of Eu-doped SrAl_2O_4 nanophosphors by CO_2 laser vaporization, Acta Mater. **61**, 7133 (2013).
- [14] J. Bierwagen, T. Delgado, J. Afshani, S. Yoon, N. Gartmann, B. Walfort, and H. Hagemann, Observation of multiple sites for trivalent europium ions in SrAl_2O_4 , J. Lumin. **239**, 118348 (2021).
- [15] J. Botterman, J. J. Joos, and P. F. Smet, Trapping and detrapping in $\text{SrAl}_2\text{O}_4\text{:Eu,Dy}$ persistent phosphors: Influence of excitation wavelength and temperature, Phys. Rev. B **90**, 085147 (2014).
- [16] C. Beauger, *Élaboration, caractérisation et modélisation des phénomènes de luminescence du monoaluminate de strontium dopé à l'euporium et au dysprosium $\text{SrAl}_2\text{O}_4\text{:Eu, Dy}$* , Ph.D. thesis, Ecole Nationale Supérieure des Mines de Saint-Etienne (1999).
- [17] T. Aitasalo, P. Dereñ, J. Hölsä, H. Jungner, J.-C. Krupa, M. Lastusaari, J. Legendziewicz, J. Niittykoski, and W. Stręk, Persistent luminescence phenomena in materials doped with rare earth ions, J. Solid State Chem. **171**, 114 (2003).
- [18] T. Aitasalo, J. Hölsä, H. Jungner, J.-C. Krupa, M. Lastusaari, J. Legendziewicz, and J. Niittykoski, Effect of temperature on the luminescence processes of $\text{SrAl}_2\text{O}_4\text{:Eu}^{2+}$, Radiat. Meas. **38**, 727 (2004).
- [19] F. Clabau, X. Rocquefelte, S. Jobic, P. Deniard, M.-H. Whangbo, A. Garcia, and T. Le Mercier, Mechanism of Phosphorescence Appropriate for the Long-Lasting Phosphors Eu^{2+} -Doped SrAl_2O_4 with Codopants Dy^{3+} and B^{3+} , Chem. Mater. **17**, 3904 (2005).
- [20] P. Dorenbos, Mechanism of Persistent Luminescence in Eu^{2+} and Dy^{3+} Codoped Aluminate and Silicate Compounds, J. Electrochem. Soc. **152**, H107 (2005).
- [21] V. Liepina, D. Millers, and K. Smits, Tunneling luminescence in long lasting afterglow of $\text{SrAl}_2\text{O}_4\text{:Eu,Dy}$, J. Lumin. **185**, 151 (2017).
- [22] P. Zeng, X. Wei, M. Yin, and Y. Chen, Investigation of the long afterglow mechanism in $\text{SrAl}_2\text{O}_4\text{:Eu}^{2+}/\text{Dy}^{3+}$ by optically stimulated luminescence and thermoluminescence, J. Lumin. **199**, 400 (2018).
- [23] J. R. N. Gnidakoung and G. J. Yun, Dislocation density level induced divergence between stress-free afterglow and mechanoluminescence in $\text{SrAl}_2\text{O}_4\text{:Eu}^{2+}, \text{Dy}^{3+}$, Ceram. Int. **45**, 1794 (2019).
- [24] J. Heyd, G. E. Scuseria, and M. Ernzerhof, Hybrid functionals based on a screened Coulomb potential, J. Chem. Phys. **118**, 8207 (2003).
- [25] C. Freysoldt, B. Grabowski, T. Hickel, J. Neugebauer, G. Kresse, A. Janotti, and C. G. Van de Walle, First-principles calculations for point defects in solids, Rev. Mod. Phys. **86**, 253 (2014).
- [26] K. Hoang, Hybrid density functional study of optically active Er^{3+} centers in GaN, Phys. Status Solidi RRL **9**, 722 (2015).
- [27] K. Hoang, First-principles identification of defect levels in Er-doped GaN, Phys. Status Solidi RRL **10**, 915 (2016).
- [28] K. Hoang, Tuning the valence and concentration of europium and luminescence centers in GaN through co-doping and defect association, Phys. Rev. Materials **5**, 034601 (2021).
- [29] C. G. Van de Walle and J. Neugebauer, First-principles calculations for defects and impurities: Applications to III-nitrides, J. Appl. Phys. **95**, 3851 (2004).
- [30] C. Freysoldt, J. Neugebauer, and C. G. Van de Walle, Fully *Ab Initio* Finite-Size Corrections for Charged-Defect Supercell Calculations, Phys. Rev. Lett. **102**, 016402 (2009).
- [31] C. Freysoldt, J. Neugebauer, and C. G. Van de Walle, Electrostatic interactions between charged defects in supercells, phys. status solidi (b) **248**, 1067 (2011).
- [32] G. Blasse and B. C. Grabmaier, *Luminescent Materials* (Springer-Verlag, Berlin, 1994).
- [33] A. Canning, A. Chaudhry, R. Boutchko, and N. Grønbech-Jensen, First-principles study of luminescence in Ce-doped inorganic scintillators, Phys. Rev. B **83**, 125115 (2011).
- [34] Y. Jia, A. Miglio, S. Poncé, M. Mikami, and X. Gonze, First-principles study of the luminescence of Eu^{2+} -doped phosphors, Phys. Rev. B **96**, 125132 (2017).
- [35] P. E. Blöchl, Projector augmented-wave method, Phys. Rev. B **50**, 17953 (1994).
- [36] G. Kresse and J. Furthmüller, Efficient iterative schemes for ab initio total-energy calculations using a plane-wave basis set, Phys. Rev. B **54**, 11169 (1996).
- [37] A. R. Schulze and M. Buschbaum, Zur Verbindungsbildung von $\text{MeO:M}_2\text{O}_3$. IV. Zur Struktur von monoklinem SrAl_2O_4 , Z. Anorg. Allg. Chem. **475**, 205 (1981).
- [38] J. Holsa, T. Laamanen, M. Lastusaari, J. Niittykoski, and P. Novak, Electronic structure of the $\text{SrAl}_2\text{O}_4\text{:Eu}^{2+}$ persistent luminescence material, J. Rare Earths **27**, 550 (2009).
- [39] D. Dutczak, T. Jüstel, C. Ronda, and A. Mei-

- jerink, Eu^{2+} luminescence in strontium aluminates, *Phys. Chem. Chem. Phys.* **17**, 15236 (2015).
- [40] M. Gajdoš, K. Hummer, G. Kresse, J. Furthmüller, and F. Bechstedt, Linear optical properties in the projector-augmented wave methodology, *Phys. Rev. B* **73**, 045112 (2006).
- [41] J. P. Perdew, K. Burke, and M. Ernzerhof, Generalized gradient approximation made simple, *Phys. Rev. Lett.* **77**, 3865 (1996).
- [42] A. Jain, S. P. Ong, G. Hautier, W. Chen, W. D. Richards, S. Dacek, S. Cholia, D. Gunter, D. Skinner, G. Ceder, and K. A. Persson, Commentary: The materials project: A materials genome approach to accelerating materials innovation, *APL Materials* **1**, 011002 (2013).
- [43] F. Massazza, The system $\text{SrO-Al}_2\text{O}_3$, *Chim. Ind. (Milan)* **41**, 108 (1959).
- [44] M. Capron and A. Douy, Strontium Dialuminate SrAl_4O_7 : Synthesis and Stability, *J. Am. Ceram. Soc.* **85**, 3036 (2002).
- [45] D. R. Stull and H. Prophet, *JANAF Thermochemical Tables*, 2nd ed. (U.S. National Bureau of Standards, Washington, D.C., 1971).
- [46] K. Momma and F. Izumi, *VESTA 3* for three-dimensional visualization of crystal, volumetric and morphology data, *J. Appl. Cryst.* **44**, 1272 (2011).
- [47] E. Finley, A. Mansouri Tehrani, and J. Brgoch, Intrinsic Defects Drive Persistent Luminescence in Monoclinic $\text{SrAl}_2\text{O}_4:\text{Eu}^{2+}$, *J. Phys. Chem. C* **122**, 16309 (2018).
- [48] G. Kaur Behrh, H. Serier-Brault, S. Jobic, and R. Gautier, A Chemical Route Towards Single-Phase Materials with Controllable Photoluminescence, *Angew. Chem. Intl. Ed.* **54**, 11501 (2015).
- [49] D. Wang, Q. Yin, Y. Li, and M. Wang, Concentration quenching of Eu^{2+} in $\text{SrO-Al}_2\text{O}_3:\text{Eu}^{2+}$ phosphor, *J. Lumin.* **97**, 1 (2002).
- [50] J. J. Joos, K. Korthout, L. Amidani, P. Glatzel, D. Poelman, and P. F. Smet, Identification of $\text{Dy}^{3+}/\text{Dy}^{2+}$ as Electron Trap in Persistent Phosphors, *Phys. Rev. Lett.* **125**, 033001 (2020).
- [51] T. Katsumata, S. Toyomane, R. Sakai, S. Komuro, and T. Morikawa, Trap Levels in Eu-Doped SrAl_2O_4 Phosphor Crystals Co-Doped with Rare-Earth Elements, *J. Am. Ceram. Soc.* **89**, 932 (2006).
- [52] K. Hoang, Rare-earth defects in GaN: A systematic investigation of the lanthanide series, *Phys. Rev. Materials* **6**, 044601 (2022).
- [53] J. Bierwagen, S. Yoon, N. Gartmann, B. Walfort, and H. Hagemann, Thermal and concentration dependent energy transfer of Eu^{2+} in SrAl_2O_4 , *Opt. Mater. Express* **6**, 793 (2016).
- [54] L. Ning, X. Huang, Y. Huang, and P. A. Tanner, Origin of the green persistent luminescence of Eu-doped SrAl_2O_4 from a multiconfigurational ab initio study of $4f^7 \rightarrow 4f^65d^1$ transitions, *J. Mater. Chem. C* **6**, 6637 (2018).
- [55] V. I. Anisimov, J. Zaanen, and O. K. Andersen, Hubbard-corrected density-functional theory, *Phys. Rev. B* **44**, 943 (1991).
- [56] J. W. Mayer and S. S. Lau, *Electronic Materials Science: For Integrated Circuits in Si and GaAs* (MacMillan Publishing, New York, 1990) p. 161.
- [57] X. Lu, W. Shu, Q. Yu, Q. Fang, and X. Xiong, Roles of doping ions in persistent luminescence of $\text{SrAl}_2\text{O}_4:\text{Eu}^{2+}, \text{RE}^{3+}$ phosphors, *Glass Phys. Chem.* **33**, 62 (2007).
- [58] J. Bierwagen, T. Delgado, G. Jiranek, S. Yoon, N. Gartmann, B. Walfort, M. Pollnau, and H. Hagemann, Probing traps in the persistent phosphor $\text{SrAl}_2\text{O}_4:\text{Eu}^{2+}, \text{Dy}^{3+}, \text{B}^{3+}$ - A wavelength, temperature and sample dependent thermoluminescence investigation, *J. Lumin.* **222**, 117113 (2020).
- [59] E. Nakazawa, Y. Murazaki, and S. Saito, Mechanism of the persistent phosphorescence in $\text{Sr}_4\text{Al}_{14}\text{O}_{25}:\text{Eu}$ and $\text{SrAl}_2\text{O}_4:\text{Eu}$ codoped with rare earth ions, *J. Appl. Phys.* **100**, 113113 (2006).
- [60] L. Razinkovas, M. Maciaszek, F. Reinhard, M. W. Doherty, and A. Alkauskas, Photoionization of negatively charged NV centers in diamond: Theory and *ab initio* calculations, *Phys. Rev. B* **104**, 235301 (2021).
- [61] C. E. Dreyer, A. Alkauskas, J. L. Lyons, and C. G. Van de Walle, Radiative capture rates at deep defects from electronic structure calculations, *Phys. Rev. B* **102**, 085305 (2020).
- [62] J. Ueda, T. Nakanishi, Y. Katayama, and S. Tanabe, Optical and optoelectronic analysis of persistent luminescence in $\text{Eu}^{2+}\text{-Dy}^{3+}$ codoped SrAl_2O_4 ceramic phosphor, *phys. stat. solidi c* **9**, 2322 (2012).

TABLE I. Formation enthalpies (calculated at 0 K, in eV per formula unit) of SrAl_2O_4 , Sr–Al–O phases that define the stability region of SrAl_2O_4 , and Eu- and Dy-related phases employed in the determination of the Eu and Dy chemical potentials.

SrAl_2O_4	$\text{Sr}_3\text{Al}_2\text{O}_6$	$\text{Sr}_4\text{Al}_{14}\text{O}_{25}$	SrO_2	SrAl_2	SrAl_4	Eu_2O_3	EuO	Dy_2O_3
-22.6974	-34.2968	-139.7826	-5.8455	-0.8403	-1.2252	-14.3794	-6.2000	-18.7462

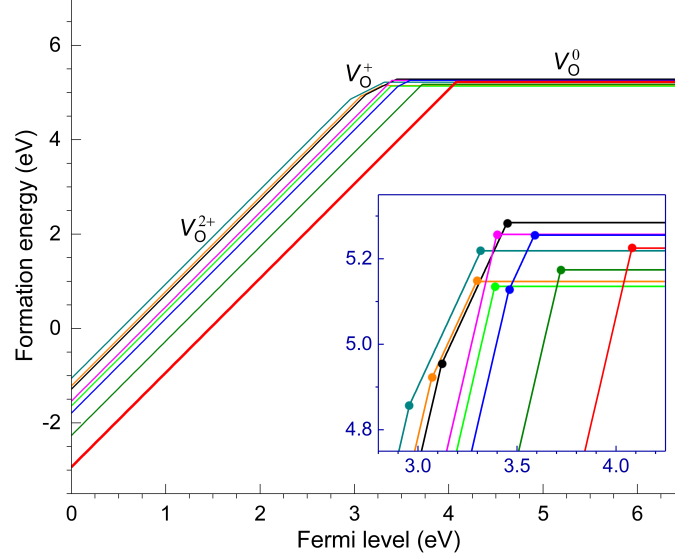


FIG. 10. Formation energies of oxygen vacancies at eight inequivalent O lattice sites in SrAl_2O_4 (see Fig. S1), as a function of the Fermi level from the VBM to the CBM, calculated at point $O1$ in the phase diagram (Fig. 1). For each defect, only segments of the formation energy lines corresponding to the lowest-energy charge states are shown. The kinks connecting two energy segments with different slopes mark the *defect levels* [i.e., thermodynamic transition levels $\epsilon(q/q')$]. The defect levels introduced by the vacancies are 2.43–3.55 eV below the CBM. The lowest-energy V_{O}^{2+} configuration occurs at the O8 site.

TABLE II. Defect energy levels (in eV, with respect to the VBM) induced by native defects and rare-earth (RE) impurities.

Defect	Lattice site	Stable RE ions	Defect energy levels
V_{O}	O8 site		$\epsilon(2+/0) = 4.08$
O_i			$\epsilon(+/0) = 1.29$, $\epsilon(0/2-) = 3.29^a$
V_{Sr}	Sr1 site		$\epsilon(+/0) = 0.95$, $\epsilon(0/-) = 1.21$, $\epsilon(-/2-) = 1.73$
	Sr2 site		$\epsilon(+/0) = 0.94$, $\epsilon(0/-) = 1.24$, $\epsilon(-/2-) = 1.73$
Sr_i	Sr1 channel		$\epsilon(3+/2+) = 0.61$, $\epsilon(2+/+) = 6.00$, $\epsilon(+/0) = 6.17$
	Sr2 channel		$\epsilon(3+/2+) = 0.65$, $\epsilon(2+/+) = 6.08$, $\epsilon(+/0) = 6.21$
Al_{Sr}	Sr2 site		$\epsilon(2+/+) = 0.24$, $\epsilon(+/-) = 5.10^b$
Sr_{Al}	Al2 site		$\epsilon(+/0) = 1.37$, $\epsilon(0/-) = 1.80$
Eu_{Sr}	Sr1 site	Eu^{3+} , Eu^{2+}	$\epsilon(+/0) = 2.69$
	Sr2 site	Eu^{3+} , Eu^{2+}	$\epsilon(+/0) = 2.79$
Eu_{Al}	Al2 site	Eu^{3+} , Eu^{2+}	$\epsilon(2+/+) = 0.75$, $\epsilon(+/0) = 0.86$, $\epsilon(+/0) = 4.87$
Dy_{Sr}	Sr1 site	Dy^{3+} , Dy^{2+}	$\epsilon(+/0) = 6.21$
	Sr2 site	Dy^{3+} , Dy^{2+}	$\epsilon(+/0) = 6.13$
Dy_{Al}	Al2 site	Dy^{4+} , Dy^{3+}	$\epsilon(2+/+) = 0.60$, $\epsilon(+/0) = 1.07$

^aThe $\epsilon(0/-)$ and $\epsilon(-/2-)$ levels are very close to the $\epsilon(0/2-)$ level, at 3.28 and 3.30 eV, respectively.

^bThe $\epsilon(+/0)$ and $\epsilon(0/-)$ levels are very close to the $\epsilon(+/-)$ level, at 5.10 and 5.09 eV, respectively.

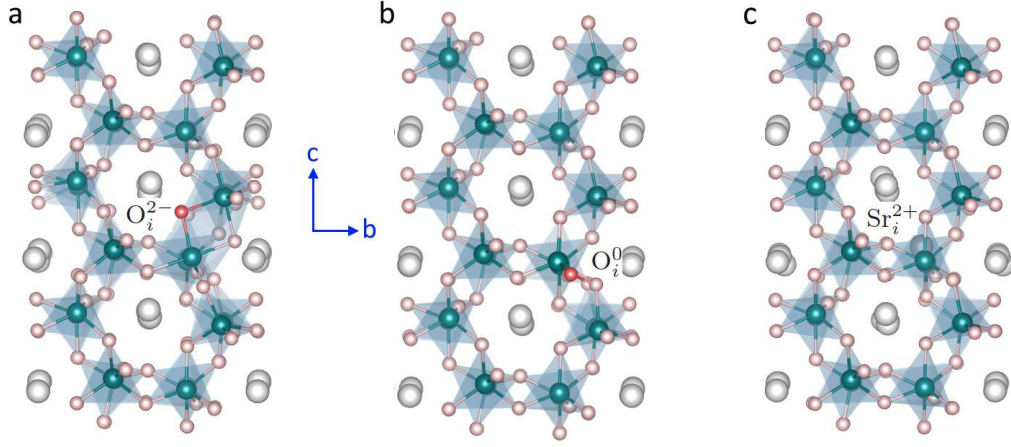


FIG. 11. A different view of (a) O_i^{2-} , (b) O_i^0 , and (c) Sr_i^{2+} (in the Sr2 channel; between two AlO_4 units when viewed along the a -axis) defect configurations in $SrAl_2O_4$. Large (gray) spheres are Sr, medium (blue) are Al, and small (red) are O.

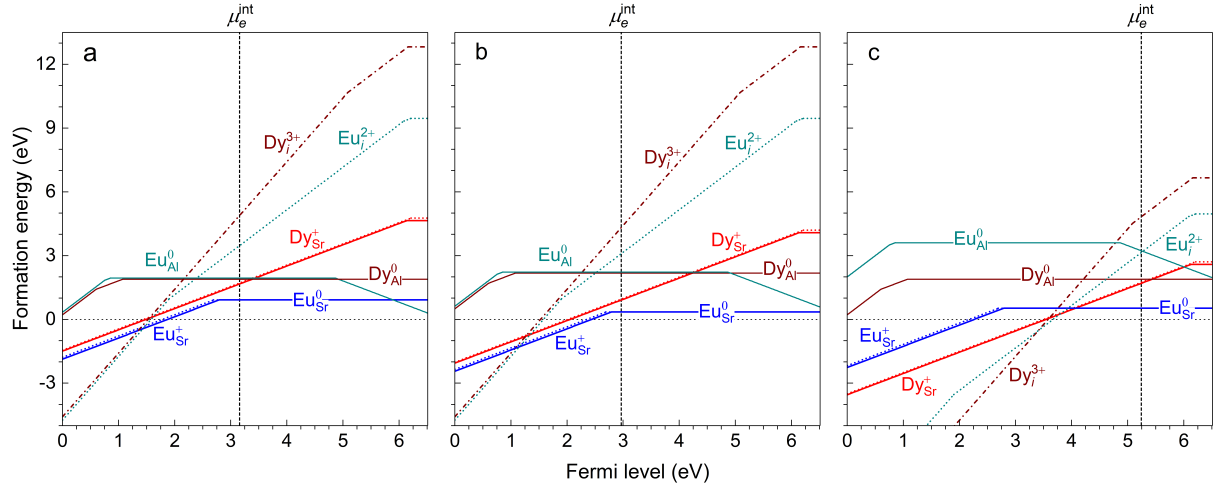


FIG. 12. Formation energies of Eu- and Dy-related defects in $SrAl_2O_4$, calculated at points (a) $O1$, (b) $O2$, and (c) R in the phase diagram (Fig. 1). The results for the Eu and Dy interstitials are also included. μ_e^{int} is the Fermi-level position determined by native point defects; see the main text. The kinks connecting two segments with different slopes mark the *defect levels*.

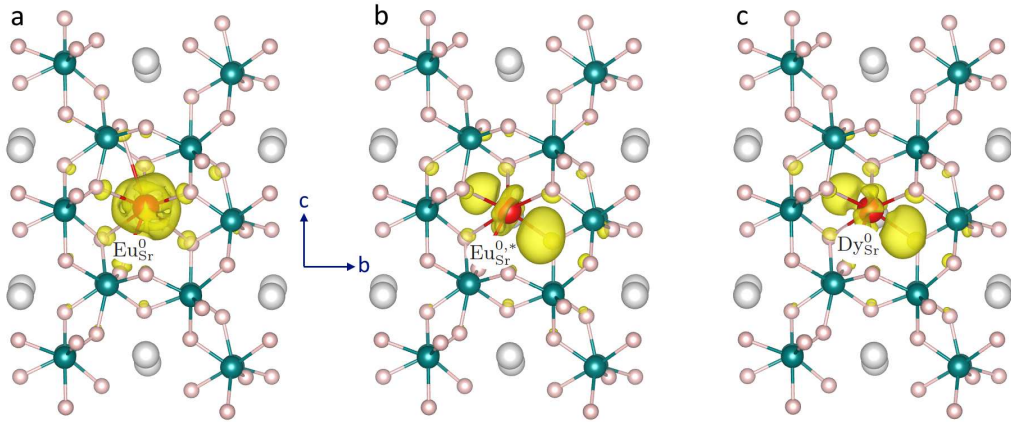
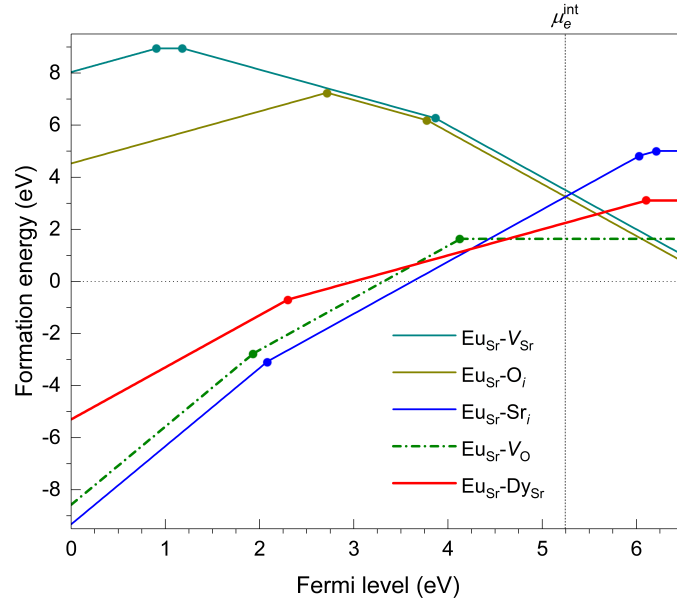


FIG. 13. Charge densities showing the localized electron residing at the highest occupied state of (a) Eu_{Sr}^0 ($4f^7$), (b) $Eu_{Sr}^{0,*}$ ($4f^6 5d^1$), and (c) Dy_{Sr}^0 ($4f^9 5d^1$); all the three defect configurations are at the Sr2 site. The isovalue for the isosurface is set to $0.03 e/\text{\AA}^3$. Larger (red) spheres are Eu/Dy, large (gray) are Sr, medium (blue) are Al, and small (red) are O.

TABLE III. Stable charge states of Eu-related defect complexes, their constituent defects, and binding energies (E_b).

Complex	Constituents	E_b (eV)	Complex	Constituents	E_b (eV)
$(\text{Eu}_{\text{Sr}}-\text{Dy}_{\text{Sr}})^{2+}$	$\text{Eu}_{\text{Sr}}^+ + \text{Dy}_{\text{Sr}}^+$	-0.41	$(\text{Eu}_{\text{Sr}}-\text{Sr}_i)^{3+}$	$\text{Eu}_{\text{Sr}}^+ + \text{Sr}_i^{2+}$	-0.69
$(\text{Eu}_{\text{Sr}}-\text{Dy}_{\text{Sr}})^+$	$\text{Eu}_{\text{Sr}}^0 + \text{Dy}_{\text{Sr}}^+$	-0.02	$(\text{Eu}_{\text{Sr}}-\text{Sr}_i)^{2+}$	$\text{Eu}_{\text{Sr}}^0 + \text{Sr}_i^{2+}$	0.01
$(\text{Eu}_{\text{Sr}}-\text{Dy}_{\text{Sr}})^0$	$\text{Eu}_{\text{Sr}}^0 + \text{Dy}_{\text{Sr}}^0$	0.01	$(\text{Eu}_{\text{Sr}}-\text{Sr}_i)^+$	$\text{Eu}_{\text{Sr}}^0 + \text{Sr}_i^+$	0.05
$(\text{Eu}_{\text{Sr}}-\text{V}_{\text{O}})^{3+}$	$\text{Eu}_{\text{Sr}}^+ + \text{V}_{\text{O}}^{2+}$	-0.73	$(\text{Eu}_{\text{Sr}}-\text{Sr}_i)^0$	$\text{Eu}_{\text{Sr}}^0 + \text{Sr}_i^0$	0.05
$(\text{Eu}_{\text{Sr}}-\text{V}_{\text{O}})^{2+}$	$\text{Eu}_{\text{Sr}}^0 + \text{V}_{\text{O}}^{2+}$	0.07	$(\text{Eu}_{\text{Sr}}-\text{V}_{\text{Sr}})^+$	$\text{Eu}_{\text{Sr}}^+ + \text{V}_{\text{Sr}}^0$	0.31
$(\text{Eu}_{\text{Sr}}-\text{V}_{\text{O}})^0$	$\text{Eu}_{\text{Sr}}^0 + \text{V}_{\text{O}}^0$	0.01	$(\text{Eu}_{\text{Sr}}-\text{V}_{\text{Sr}})^0$	$\text{Eu}_{\text{Sr}}^+ + \text{V}_{\text{Sr}}^-$	0.61
$(\text{Eu}_{\text{Sr}}-\text{O}_i)^+$	$\text{Eu}_{\text{Sr}}^+ + \text{O}_i^0$	-0.06	$(\text{Eu}_{\text{Sr}}-\text{V}_{\text{Sr}})^-$	$\text{Eu}_{\text{Sr}}^+ + \text{V}_{\text{Sr}}^{2-}$	1.15
$(\text{Eu}_{\text{Sr}}-\text{O}_i)^-$	$\text{Eu}_{\text{Sr}}^+ + \text{O}_i^{2-}$	1.09	$(\text{Eu}_{\text{Sr}}-\text{V}_{\text{Sr}})^{2-}$	$\text{Eu}_{\text{Sr}}^0 + \text{V}_{\text{Sr}}^{2-}$	0.07
$(\text{Eu}_{\text{Sr}}-\text{O}_i)^{2-}$	$\text{Eu}_{\text{Sr}}^0 + \text{O}_i^{2-}$	0.00			

FIG. 14. Formation energies of possible Eu-related defect complexes in SrAl_2O_4 , calculated at point R in the phase diagram (Fig. 1). The two constituent defects in a complex are nearest neighbors to each other. μ_e^{int} is the Fermi-level position determined by native point defects. The solid dots connecting two energy segments with different slopes mark the *defect levels*.TABLE IV. Peak absorption energy (E_{abs}), peak emission energy (E_{em}), Franck-Condon shifts ($d_{\text{FC}}^{\text{e,g}}$), Stokes shift (ΔS), and thermal energy (E_{therm}) associated with the Eu-related band-defect and $5d-4f$ optical transitions; all in eV.

Lattice site	E_{abs}	d_{FC}^{e}	E_{em}	d_{FC}^{g}	ΔS	E_{therm}	E_{abs}	d_{FC}^{e}	E_{em}	d_{FC}^{g}	ΔS	E_{therm}
HSE: $\text{Eu}_{\text{Sr}}^0 \rightleftharpoons \text{Eu}_{\text{Sr}}^+ + e^-$							HSE: $\text{Eu}_{\text{Sr}}^0 (4f^7) \rightleftharpoons \text{Eu}_{\text{Sr}}^{0,*} (4f^6 5d^1)$					
Sr1	4.86	1.04	2.71	1.11	2.15	3.82	3.91	0.22	3.42	0.27	0.49	3.69
Sr2	4.71	0.98	2.70	1.02	2.00	3.72	3.69	0.28	3.05	0.36	0.64	3.41
HSE: $\text{Eu}_{\text{Sr}}^+ \rightleftharpoons \text{Eu}_{\text{Sr}}^0 + h^+$							DFT+ U : ^a $\text{Eu}_{\text{Sr}}^0 (4f^7) \rightleftharpoons \text{Eu}_{\text{Sr}}^{0,*} (4f^6 5d^1)$					
Sr1	3.80	1.11	1.65	1.04	2.15	2.69	4.23	0.32	3.52	0.39	0.61	3.91
Sr2	3.81	1.02	1.81	0.98	2.00	2.79	4.00	0.29	3.38	0.33	0.72	3.71

^aDFT+ U calculations with a computational setup similar to that in Jia et al., Phys. Rev. B **96**, 125132 (2017); see text.